Microwave engineering of plasma-assisted CVD reactors for diamond deposition

2009 J. Phys.: Condens. Matter 21 364202

(http://iopscience.iop.org/0953-8984/21/36/364202)

J. Phys.: Condens. Matter **21** (2009) 364202 (16pp) doi:10.1088/0953-8984/21/36/364202

Microwave engineering of plasma-assisted CVD reactors for diamond deposition

F Silva, K Hassouni, X Bonnin and A Gicquel

LIMHP, Université Paris 13, CNRS, Institut Galilée, 99 avenue Jean-Baptiste Clément, F-93430 Villetaneuse, France

E-mail: silva@limhp.univ-paris13.fr

Received 9 April 2009, in final form 5 May 2009
Published 19 August 2009
Online at stacks.iop.org/JPhysCM/21/364202

Abstract

The unique properties of CVD diamond make it a compelling choice for high power electronics. In order to achieve industrial use of CVD diamond, one must simultaneously obtain an excellent control of the film purity, very low defect content and a sufficiently rapid growth rate. Currently, only microwave plasma-assisted chemical vapour deposition (MPACVD) processes making use of resonant cavity systems provide enough atomic hydrogen to satisfy these requirements.

We show in this paper that the use of high microwave power density (MWPD) plasmas is necessary to promote atomic hydrogen concentrations that are high enough to ensure the deposition of high purity diamond films at large growth rates. Moreover, the deposition of homogeneous films on large surfaces calls for the production of plasma with appropriate shapes and large volumes. The production of such plasmas needs generating a fairly high electric field over extended regions and requires a careful design of the MW coupling system, especially the cavity.

As far as MW coupling efficiency is concerned, the presence of a plasma load represents a mismatching perturbation to the cavity. This perturbation is especially important at high MWPD where the reflected fraction of the input power may be quite high. This mismatch can lead to a pronounced heating of the reactor walls. It must therefore be taken into account from the very beginning of the reactor design. This requires the implementation of plasma modelling tools coupled to detailed electromagnetic simulations. This is discussed in section 3.

We also briefly discuss the operating principles of the main commercial plasma reactors before introducing the reactor design methodology we have developed. Modelling results for a new generation of reactors developed at LIMHP, working at very high power density, will be presented. Lastly, we show that scaling up this type of reactor to lower frequencies (915 MHz) can result in high density plasmas allowing for fast and homogeneous diamond deposition on up to 160 mm diameter surfaces.

(Some figures in this article are in colour only in the electronic version)

1. Introduction

The significant progress made on CVD diamond synthesis these last few years, especially with respect to purity and crystalline defect content [1–5], generated new interest in this material for a large number of applications. However, CVD diamond production at high growth rates and on large areas remains a critical prerequisite for industrial usage. In this respect, reactor performance plays an essential role.

The first part of this paper is dedicated to the influence of the deposition process parameters, and more particularly the MWPD, on the production rate of the growth species and CVD diamond growth kinetics. From these results, a number of recommendations that would hopefully enable one to obtain simultaneously large growth rates and high film quality can be made.

The second part of this paper deals with the design of plasma reactors that make use of a resonant cavity. We present a detailed methodology based on microwave engineering and plasma modelling and which allowed us to develop microwave plasma reactors that operate in a very stable fashion at very

high MWPD. This new generation of plasma devices prevents overheating of the reactor walls and other system components.

2. CVD diamond growth key parameters

CVD diamond growth is a complex process, the full description of which is rather difficult. It requires knowing the gas composition in front of the growing surface and describing the details of surface kinetics including adsorption–desorption, abstraction and migration phenomena. The complexity of the surface structure made up of steps and terraces and subject to reconstruction processes has also to be taken into account. Although there is currently no model that describes all aspects of CVD diamond growth, some simplified approaches do provide an understanding of the influence of some deposition process parameters on some features of the growth kinetics.

The model proposed by Harris and Goodwin [6–8] describes the growth of CVD diamond in a very simple way. This model assumes that diamond growth involves only two species, H and CH_3, and five reactions. The diamond growth proceeds by incorporation of growth units consisting of methyl radicals. This incorporation is made possible by the creation of open sites available for growth (denoted Cd^*). This is ensured by the abstraction of the hydrogen atoms chemisorbed on the diamond surface. The main abstraction process is induced by H atoms generated in the gas phase and results in the formation of H_2 molecules. The CH_3 radical can be adsorbed on the site opened by the abstraction process. It then undergoes subsequent abstraction reactions to become fully integrated in the diamond lattice. From this simplified kinetic scheme, where the fundamental roles of atomic hydrogen emerge, it is possible to derive an expression for the growth rate $G_{\{100\}}$ of {100} diamond planes which depends on the H and CH_3 surface concentrations (equation (1), see [6–8] for notation) :

$$G_{\{100\}} = k_3 \frac{n_s}{n_d} \left(\frac{k_1}{k_1 + k_2} \right) \frac{[CH_3]_s\,[H]_s}{\frac{k_4}{k_5} + [H]_s}. \qquad (1)$$

We have developed two plasma models to compute the gas phase concentrations of H and CH_3 as a function of the deposition parameters (pressure, microwave power, methane concentration). These model results were then used to infer the effect of the process parameters on the CVD diamond growth kinetics. The first model is a 2D self-consistent plasma model [9, 10] that accurately describes all the physico-chemical phenomena taking place in a pure hydrogen microwave plasma (electromagnetic coupling, energy transfer, chemistry and transport). It yields the spatial distribution of all relevant plasma properties, such as atomic hydrogen and electron densities, gas and electron temperatures, microwave power density, etc, for an axisymmetrical reactor geometry.

Figure 1 shows the evolution of the distribution of these quantities, in our laboratory reactor (described in section 3.4 below), for a working pressure that ranges from 50 to 300 mbar. The MW power has been adjusted at each pressure so as to maintain a constant plasma volume. We first observe that the power is deposited non-uniformly in the plasma. An enhanced power deposition is especially obtained near the substrate surface. This phenomenon, which was previously described in [11], is the consequence of the Poynting vector distribution around the plasma that leads to a radial penetration of the microwaves in the discharge.

We also notice that the electron temperature drops from 15 000 to 10 000 K within this pressure range. This is due to the increase in electron–heavy species collision frequency which results in an enhanced energy transfer from the electron to heavy species with a subsequent increase of the gas temperature that varies from 2200 to 3600 K. Considering the contributions of the different reactions to the H production rate, one can show that, at low pressure, H is mainly produced by direct electron-impact dissociation ($e^- + H_2 \rightarrow e^- + 2H$) while it is mainly produced by thermal dissociation of H_2 molecules ($H_2 + H \rightarrow 3H$) at high pressure [11], as can be seen in figure 2(a). This result clearly shows that the large increase in atomic hydrogen density at high pressure is linked to the rise of gas temperature that varies by more than 1400 K.

As far as CH_3 production is concerned, we used a 1D model that describes the coupled phenomena of chemistry, energy transfer, species and energy transport in a hydrogen/methane plasma. The model takes into account 28 species and 130 reactions [12]. It requires some input data related to the process control parameters, the collision frequencies and the transport coefficients. It assumes that the microwave power density distribution is similar to the one obtained for pure H_2 plasma using the 2D self-consistent model. The results showed that CH_3 production at low pressure takes place in the plasma bulk. Its kinetics is governed by H-atom concentration (through the reaction $CH_3 + H + M \leftrightarrows CH_4 + M$, M being a third body; cf figure 2(b)).

At high pressure, CH_3 production is still due to CH_4 dissociation through collisions with H atoms, via the reaction $CH_4 + H \leftrightarrows CH_3 + H_2$. It mainly takes place very close to the surface (see the inset in the right panel of figure 2(b)). In fact, the production rate of CH_3 also depends on the gas temperature. An optimal CH_3 production is obtained for gas temperature values in the range 1200–2200 K. Such a temperature range corresponds, for the working pressure considered here, to a plasma region that is located no more than a few millimetres above the substrate surface, as illustrated in figure 3.

For the LIMHP reactors used for monocrystalline diamond deposition (cf figure 19), we plotted the evolution of the operating point in terms of H-atom and CH_3-radical surface concentrations, as introduced by Goodwin [8], for different pressure and input power discharge conditions. This diagram, represented in figure 4, shows the lines of constant growth rate and quality (cf equation (1)). The film quality is defined as the sp_2 defect density that is proportional to $G_{\{100\}}/[H]_s^2$ [8]. Different diamond deposition processes can be compared using this kind of map. Using our modelling results, it is possible to follow the operating point of our deposition process as a function of the working pressure and the methane concentration. For 1% methane in the feed gas, the increase of the pressure from 50 to 300 mbar leads to a three orders of magnitude increase of the atomic hydrogen concentration at the surface and one order of magnitude increase of CH_3

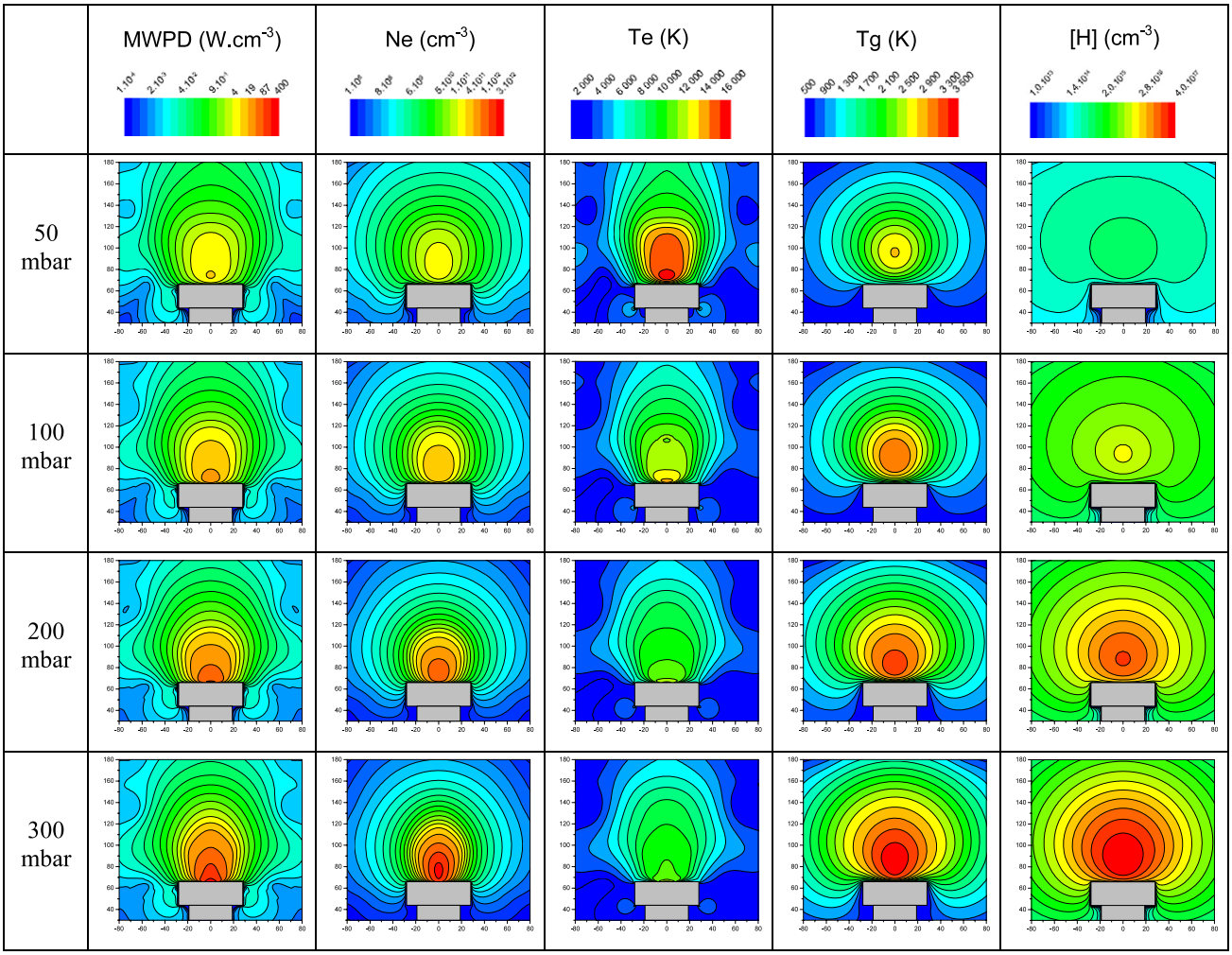

Figure 1. From left to right, spatial distributions of microwave power density (MWPD), electron density (N_e), electron temperature (T_e), gas temperature (T_g) and atomic hydrogen density ([H]) for a pure hydrogen plasma ignited inside the LIMHP reactor (cf figure 19), for different working pressures, obtained from our self-consistent H-only plasma model (MWPD, N_e and [H] are shown on a logarithmic scale). For each working pressure, the MW power was tuned so as to maintain a constant plasma volume.

concentration. This results in a growth rate of several tens of μm h^{-1} at 300 mbar. Also, it is worth mentioning that increasing methane concentration at high pressure leads to a significant increase of the growth rate without compromising the film quality.

The methane concentration that can be used in the process described here cannot exceed an upper limit of about 10%. This limit is imposed by the occurrence of soot formation at high methane concentration, which can deteriorate the film quality, thus leading to a strong decrease in the process performance. The process map shows all the advantages of working at the highest possible pressure. This allows increasing simultaneously the growth rate and the film quality. As a practical example, we have achieved deposition of high purity films at a growth rate exceeding 70 μm h^{-1} when working at high pressure (>400 mbar) [13].

However, the use of high power density plasmas often leads to a strong heating of the reactor metallic walls. It may also damage the quartz window at the top of the reduced pressure vessel where the plasma is ignited. The reactor must therefore be carefully designed to provide stable process conditions at high microwave power density and over long deposition times.

In summary, we can see that the use of MW as the production means for atomic hydrogen is especially advantageous for several reasons. First, MW plasmas promote high gas temperatures (>3200 K) as needed for an efficient H production by thermal dissociation of H_2, unlike for example hot filament sources which are limited to around 2500 K. Second, as we will see in section 3 and illustrated by figure 4, MW reactors allow for design flexibility which can be used to improve plasma homogeneity over large surfaces and simultaneously obtain large growth rates. The careful design steps needed to achieve such reactor performance will be the main topic of the remainder of this paper.

3. Microwave plasma reactor design

Unlike for most other materials, plasma-assisted CVD requires relatively high pressures in the case of diamond. For this

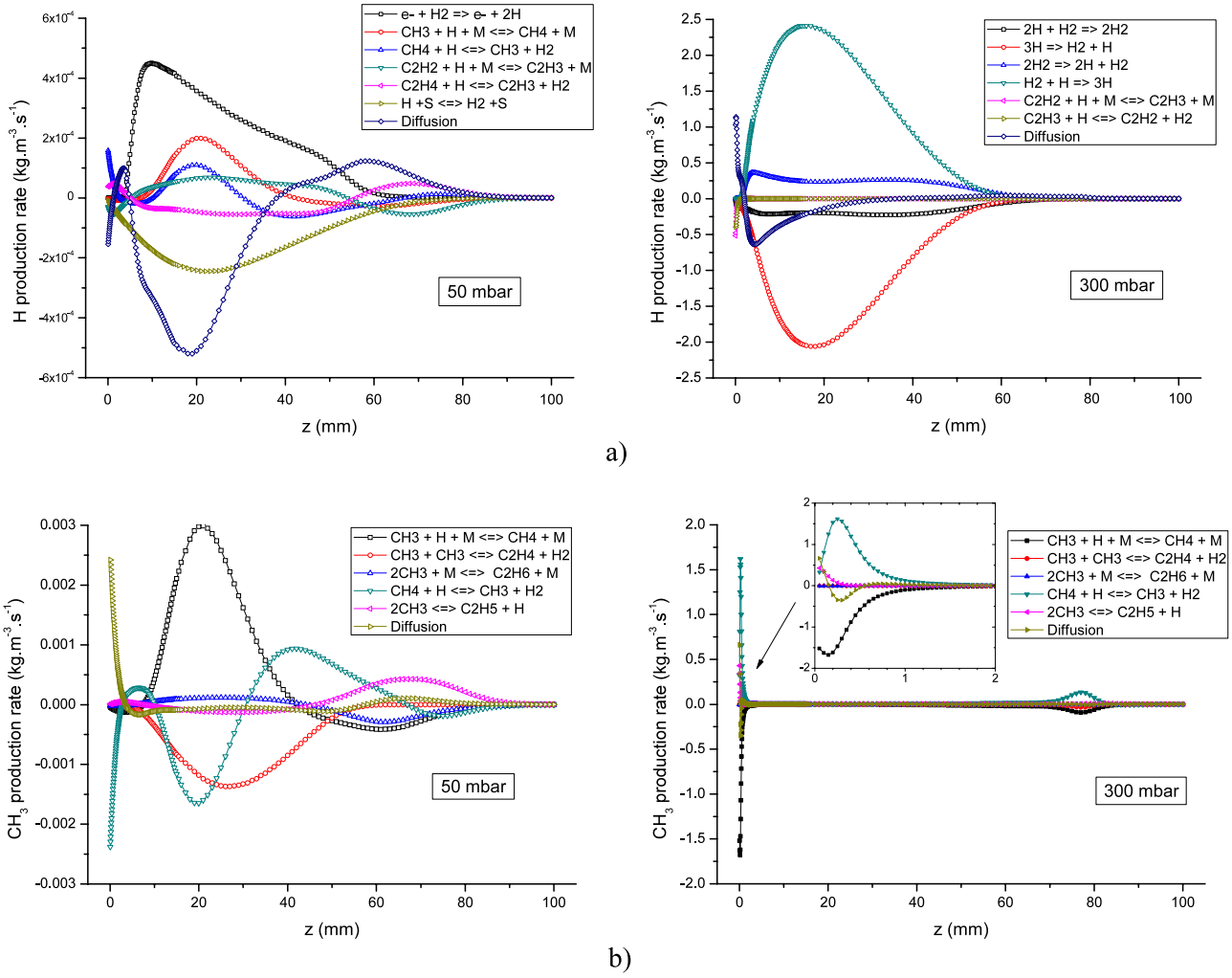

Figure 2. Axial balance of (a) atomic hydrogen and (b) CH_3 radicals for working pressures of 50 mbar (left) and 300 mbar (right), derived from the 1D H_2/CH_4 model. These results were obtained with 4% methane concentration in the feed gas.

reason, diffusion phenomena are limited and it is necessary to produce the plasma (and therefore the associated high electric field region) near the deposition substrate. Moreover, the high gas temperatures and the large thermal conductivity of hydrogen yield large heat fluxes at the reactor walls which must be dealt with. Hence, resonant electromagnetic cavities with appropriate field structures are used for the construction of diamond deposition microwave plasma reactors.

3.1. Basic principles of MW plasma reactors based on resonant cavities

One of the first advantages of this type of cavity comes from the resonance phenomenon itself. Indeed, when an electromagnetic cavity is excited at its resonant frequency (which depends on the geometry and dielectric content), it can hold a much higher electric field, thus providing easier plasma ignition. Another advantage of a resonant cavity resides in the electric field structure, which can be appropriately chosen to promote a high electric field in the low pressure region where the plasma is to be ignited without using electrodes. The skill in designing plasma reactors resides in matching the electric field structure so as to locally enhance the field strength in front of the substrate and to obtain the largest possible region with an enhanced and uniform field. A major difficulty is due to the presence of the plasma load that perturbs the cavity tuning and which must be taken into account from the beginning. We will come back later to the challenge of anticipating the cavity mismatch due to the plasma, particularly at high pressure.

There are two resonance mode types, TE and TM, depending on whether the electric or magnetic field, respectively, is orthogonal to the cavity axis. The boundary conditions on the cavity metal walls impose zero tangential components for the electric field, which forces the field to be normal to the surface. Consequently, transverse electric modes cannot have high electric field regions in contact with the metallic walls (cf figure 5), which means that the ignited plasmas will not be in contact with the substrate holder.

For this reason, transverse magnetic modes are often used in plasma reactor design and in particular TM_{0mn} modes are the most suitable. The first index for the mode number (here 0) indicates that the electric field structure is axisymmetric, which will yield a circular plasma. The indices m and n represent the number of electric field maxima (or lobes) in the radial

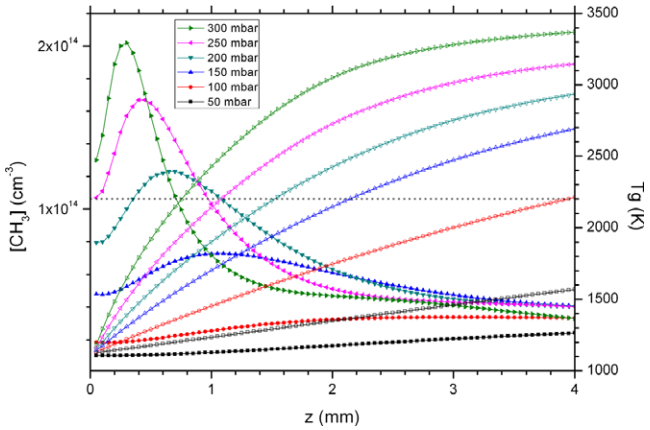

Figure 3. Evolution of the CH_3 density (full symbols, left-hand scale) and of the gas temperature (empty symbols, right-hand scale) axial profiles obtained for the LIMHP reactor (cf figure 19) from the 1D H_2/CH_4 model. The methane concentration is kept fixed at 4% and the pressure ranges from 50 to 300 mbar. The dotted line indicates the threshold temperature of 2200 K, below which CH_3 radicals can form. Note that, for each discharge condition, production of CH_3 starts when the gas temperature decreases below the threshold value of 2200 K.

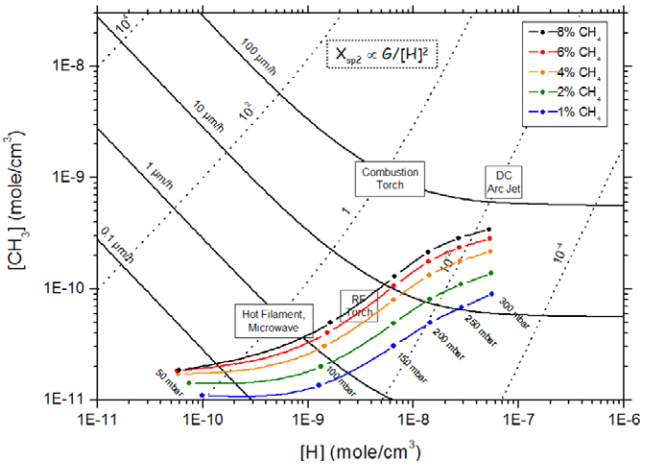

Figure 4. Process map in $[CH_3]$–$[H]$ space showing the operating ranges of the main CVD diamond growth processes (from [8]). The evolution of the operating point of the LIMHP reactor (cf figure 19) as a function of working pressure (from 50 to 300 mbar) and methane concentration (from 1 to 8%) has been added.

and axial directions, respectively. Figure 6 shows the structure of TM_{0mn} modes with the m index ranging from 1 to 3, and for the n index varying from 0 to 3. The modes surrounded by a red dashed line have been used for the design of various reactors [9, 14–22], some of which will be described below.

3.2. MW cavity coupling techniques

In this section, we will address MW cavity coupling techniques, by which the selected resonant mode is excited and MW energy can be efficiently transmitted from the power supply to the plasma load. One must make sure that the exciting field, either electric or magnetic, possesses at least one component that is similar to the field of the cavity mode that we wish to excite. We can differentiate between the electric coupling usually performed through an antenna, and the magnetic coupling that can be achieved with either a magnetic loop or slots. Let us first examine the case of electric coupling. Figure 7 shows the electric field structure of the TM_{012} resonant cavity mode by itself and the structure of the resultant cavity field excited by an antenna through a coaxial port. We clearly see the continuity of the electric field between the antenna and the cavity, and we can observe that the resonance mode is efficiently excited. This is the most commonly used coupling technique found in commercial MW plasma reactors.

Let us now consider magnetic coupling for MW cavities. Magnetic coupling, achieved via magnetic loops positioned on the cavity side walls (in order to make the magnetic field induced by the coil oriented in the same direction as the magnetic field of the cavity mode to be excited), is rarely used because of the limited power that can be coupled. Indeed, the power being carried by a coaxial cable cannot exceed about 100 W. This technique was improved by the use of slots, which allows for larger power coupling and avoids the use of coils that cause some perturbations of the local electric field inside the cavity.

Another example of a cavity system is the one shown in figure 8. It uses the TM_{012} resonant mode. The coupling is achieved with a toroidal waveguide, the length of which is an integer number of guided wavelengths (4 in this case). The waveguide is connected to the cavity through slots. This reactor is commercialized by the IPLAS Company [23]. EM simulations show that the TM_{012} mode is excited effectively inside the cavity. The magnetic field distribution depicted in figure 9 gives an understanding of how the cavity is coupled. The magnetic field in the waveguide switches from clockwise to counterclockwise rotation every half-wavelength. The openings along the waveguide are located so as to select the sections where the magnetic field in the waveguide rotates in the same direction as the magnetic field of the cavity mode to be excited.

An essential element associated with both electric and magnetic coupling schemes is the dielectric window. It is generally made of quartz and delimits a reduced pressure zone inside the cavity. It is easy to understand the need for such a window by observing the electric field distributions shown in figures 7 and 8. In the absence of such a window, all of the cavity will experience the same pressure and the plasma will be ignited in the regions with high electric field that are generally located near the coupling element that transfers the power from the excitation field to the cavity mode (near the antenna in figure 7 and along the slots in figure 8). This is, of course, often not desirable. The use of the quartz window allows us to properly select a single region of maximum electric field in the reduced pressure zone (near the substrate surface). The plasma can be ignited only in this region and the formation of parasitic plasmas can be avoided.

From a purely electromagnetic standpoint, there are three main design steps to a resonant cavity microwave plasma reactor. These are: (i) the choice of the resonant mode with an appropriate electric field structure, (ii) the choice of the

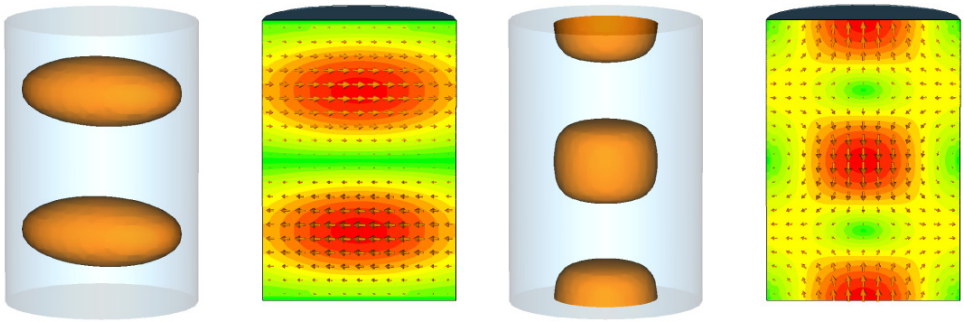

Figure 5. Example showing the electric field distribution of TE and TM modes (here, TE_{112} on the left and TM_{012} on the right) in a cylindrical cavity. For each mode, we represent iso-surfaces of field strength and a vector plot in the cavity longitudinal cut plane.

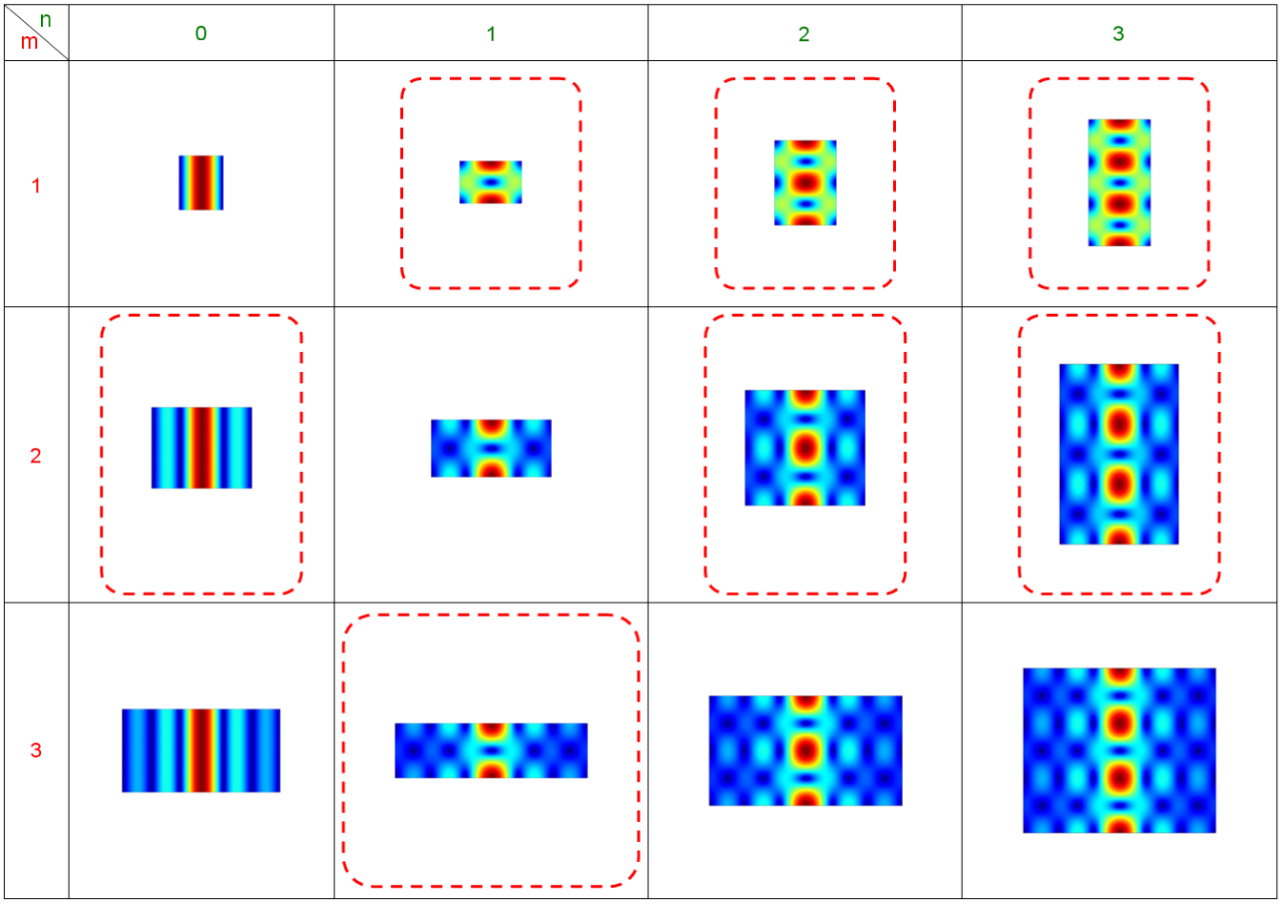

Figure 6. Details of the electric field distribution in TM_{0mn} cylindrical cavity modes, for m and n indices ranging respectively from 1 to 3 and from 0 to 3. The cavities were dimensioned so that their resonant frequencies remain identical and are to scale. Modes surrounded by a red dashed line have already been used for reactor design [9, 14–22].

coupling structure (which can be either electric or magnetic) and (iii) the choice of the dielectric window (shape and location). The main commercial reactors used for diamond deposition have been designed according to the principles above.

3.3. Overview of the main MPACVD diamond growth reactors

The various MPACVD reactors can be differentiated according to the resonance mode chosen, the coupling technique and the shape and location of the quartz window used.

In the case of the reactor shown in figure 7, the reduced pressure zone is inside a quartz bell jar. This is positioned so as to have only the lower maximum field lobe of the cavity mode inside the low pressure zone. Figure 10 illustrates the different steps of this designing principle for this bell jar type reactor initially designed at Michigan State University [15, 16]. Figure 10(d) shows the spatial distribution of H-atom density obtained at 200 mbar as predicted from the simulations of this cavity using the self-consistent model discussed previously. Because the reactor dimensions used in the simulations were

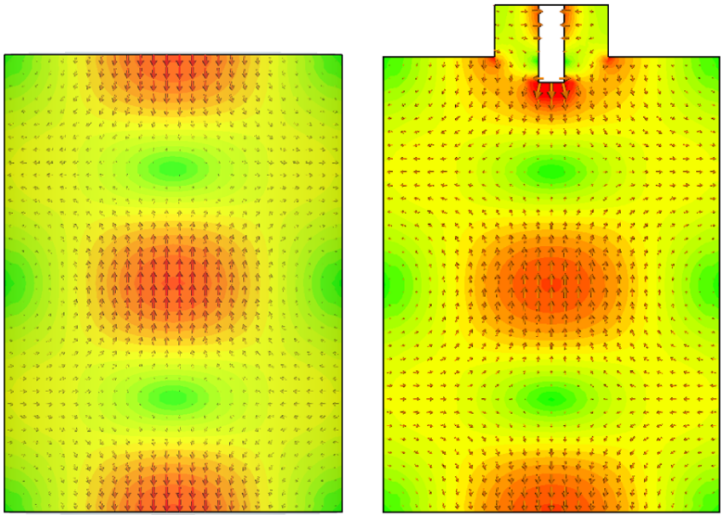

Figure 7. Illustration of the resonant cavity electric coupling technique, with excitation from an antenna. The mode considered here is TM_{012} for a cylindrical cavity, with its field structure shown on the left. The antenna is introduced at the top of the cavity through a coaxial port (right) and produces an intense electric field in the direction common with the mode field structure.

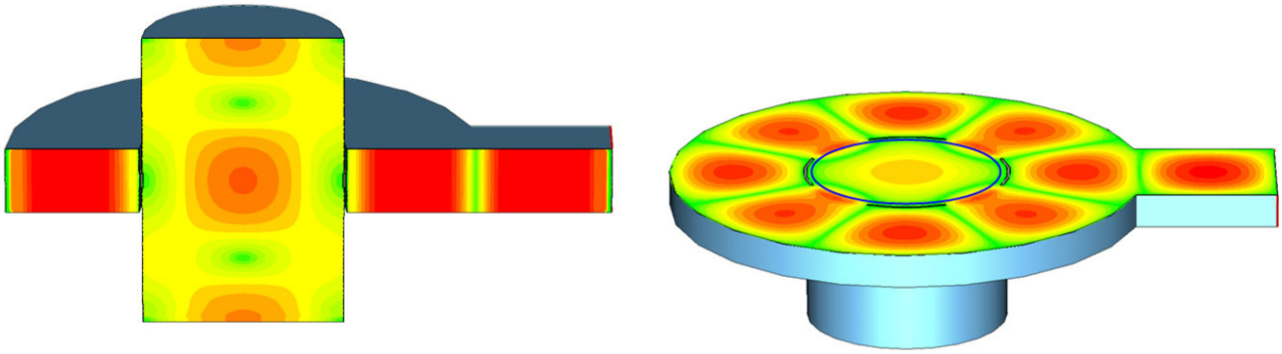

Figure 8. Illustration of the magnetic coupling technique for resonant cavities, through the use of slots, here arranged along the cavity vertical wall with a toroidal waveguide. The mode considered in this example is TM_{012} for a cylindrical cavity. The waveguide length is an integer number of guided wavelength (here 4) and the slots are positioned every other half-wavelength. The quartz window in this reactor consists of a tube located inside the cavity to avoid plasma ignition at the slot's location. This reactor is developed commercially by the IPLAS Company [23].

roughly estimated from the paper published by the group at MSU, this simulation should be considered only as an illustrative example. This will also be the case for the other commercial reactors considered in this paper.

One of the most commonly used plasma reactors is the ASTEX system (now called SEKI) which makes use of a TM_{013} mode and an antenna coupling system [17]. The peculiarity of this reactor comes from its dielectric window, which is a plate that is positioned far from the plasma in order to prevent overheating (cf figure 11).

The last generation of ASTEX reactor uses a non-cylindrical cavity [14]. This reactor presents several peculiarities. The main mode excited in this cavity is the TM_{011} mode, as imposed by the central cylindrical component. However, we also find secondary radial lobes which are related to a TM_{021} mode type (cf figure 12). This cavity is therefore a multimode cavity. The microwaves are injected from the bottom of the cavity (cf figure 12). The dielectric window, here a quartz tube, is not directly exposed to the plasma, which gives this reactor excellent power handling capabilities. Plasma modelling shows that the discharge is quite extended in size, which can be explained by the peculiar field structure in this cavity.

Another example of a reactor with a non-cylindrical cavity is the AIXTRON reactor, developed at the Fraunhofer Institute [24, 25], which uses an ellipsoidal cavity. Despite its large dimensions, this innovative cavity shape has the advantage of showing only two main field maxima, located at the foci of the ellipsoid (cf figure 13).

Figure 14 shows how the TM_{012} field distribution from a cylindrical cavity evolves when the cavity transitions from a cylindrical to an ellipsoidal geometry. The sequence of three field maxima along the cylindrical cavity axis is transformed into two main maxima located at the foci separated by a smaller secondary maximum for the ellipsoidal cavity. The reactor cavity mode can thus be similarly derived from the cylindrical TM_{036} resonance mode. Generally, the transition from a cylindrical cavity to an ellipsoidal cavity results in the

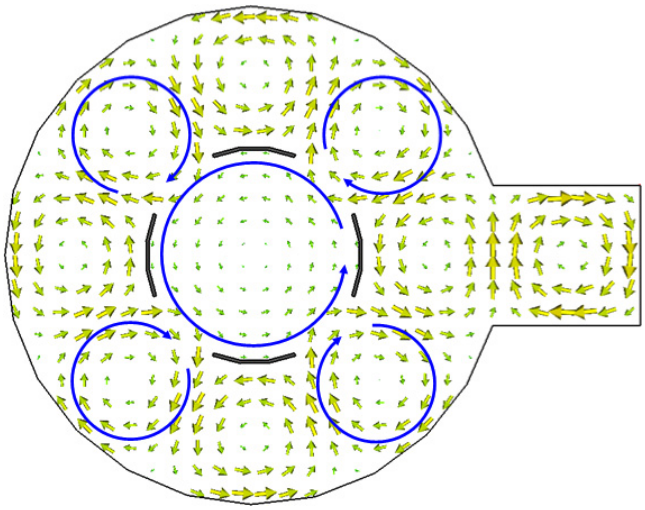

Figure 9. Details of the magnetic field distribution in a transverse cut plane for the cavity from figure 8, showing the magnetic coupling principle. The cavity openings are chosen to only select the waveguide sections where the magnetic field is rotating in the same direction as the cavity field, thereby exciting the resonance mode.

weakening of all the field maxima except the two maxima located at the foci.

From the practical point of view, the coupling in the ellipsoidal cavity is achieved through an antenna at one of the foci while the plasma is ignited at the other focus. This configuration allows for a large quartz bell jar which moves the quartz walls away from the plasma, as shown in the plasma simulation of figure 13.

3.4. Influence of the plasma on cavity behaviour

We have discussed the principles of plasma reactor design from a purely electromagnetic point of view. However, the electric field structure inside the cavity also depends on its dielectric content, namely the plasma load. In this section, we follow the analysis made in [10] to examine the incidence of the presence of such a complex dielectric medium on the cavity behaviour.

As with any other isotropic medium, an electromagnetic wave propagating in a plasma is transverse (i.e. **E** and **H** are orthogonal to the wavevector $\boldsymbol{k}$). If one neglects the collisions between particles, the dispersion relation for a wave propagating at a frequency $f = \omega/2\pi$, in a non-magnetized homogeneous plasma with electron density n_e, is given by

$$\omega^2 = \omega_P^2 + c^2k^2 \qquad \text{with } \omega_p = \sqrt{n_e \frac{e^2}{m_e \varepsilon_0}} \tag{2}$$

where ω_P is the plasma frequency, c the speed of light, m_e and e the electron mass and charge respectively, and ε_0 the vacuum permittivity [26]. We can then introduce the plasma permittivity ε_P (through the phase velocity $v_{ph} = c/\sqrt{\varepsilon_P} = \omega/k$):

$$\varepsilon_P = \varepsilon_0(1 - (\omega_P/\omega)^2). \tag{3}$$

This relationship allows us to define the critical electronic density, at a given frequency, called the cutoff plasma density, for which the plasma permittivity vanishes:

$$n_c = \varepsilon_0 m_e \omega^2/e^2. \tag{4}$$

For a frequency of $\omega/2\pi = 2.45$ GHz, the critical density n_c is equal to 7.45×10^{10} cm^{-3} (this density becomes 1.04×10^{10} cm^{-3} at 915 MHz). If one now takes into account electron–neutral collisions, through the collision frequency ν, the plasma permittivity can be written as

$$\varepsilon_P = \varepsilon_0\left(1 - \frac{(\omega_P/\omega)^2}{1 + i(\nu/\omega)}\right) \tag{5}$$

where ν can be approximated for a pure hydrogen discharge with $10^{12}\,(P_{(mbar)}/T_{g(K)})$ [16]. The previous expression can be rewritten to emphasize the real and imaginary parts of ε_P:

$$\varepsilon_P = \varepsilon_0(\varepsilon' - i\varepsilon'') = \varepsilon_0\left(1 - \frac{(\omega_P/\omega)^2}{1 + (\nu/\omega)^2}\right) - i\varepsilon_0\left(\frac{(\nu/\omega)(\omega_P/\omega)^2}{1 + (\nu/\omega)^2}\right). \tag{6}$$

The wavenumber k is related to plasma permittivity through the following expression:

$$k^2 = k_0^2(\varepsilon_P/\varepsilon_0). \tag{7}$$

An electromagnetic wave will propagate in a plasma over long distances (i.e. with relatively little damping), if $n_e < n_c$, or

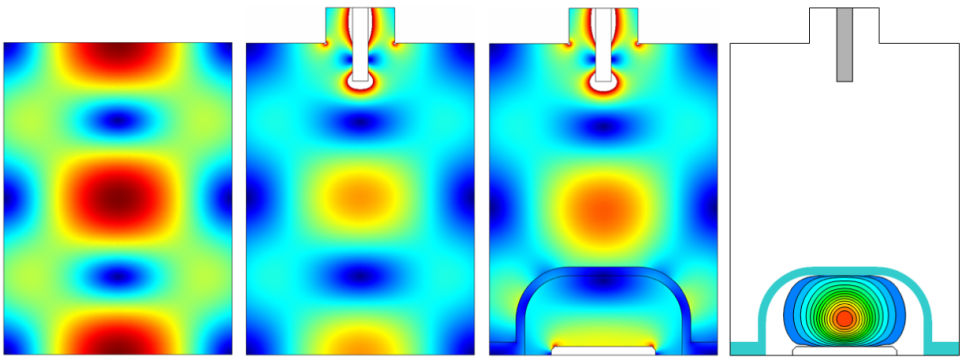

Figure 10. Different design steps for a microwave plasma reactor (example of the MSU reactor [15, 16]): (from left to right) choice of the cavity mode (TM_{012}); introduction of the MW coupling system; introduction of the dielectric window (quartz bell jar) and modelling of pure H_2 plasma at 200 mbar obtained with our self-consistent model.

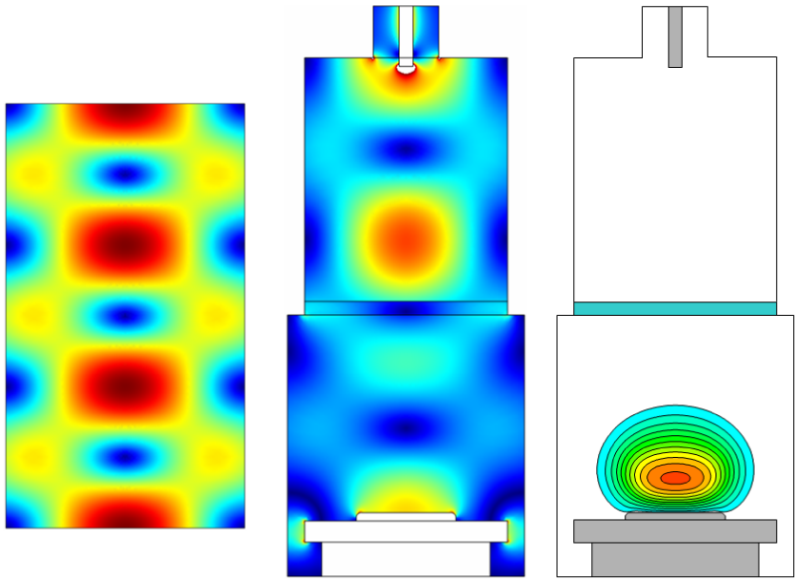

Figure 11. Illustration of the design principle for the ASTEX reactor using a TM_{013} resonant mode (left panel). The coupling is provided by an antenna and the dielectric window is a quartz plate located approximately at the cavity mid-plane [17] (central panel). In the rightmost panel, we present modelling of a 200 mbar H_2 plasma.

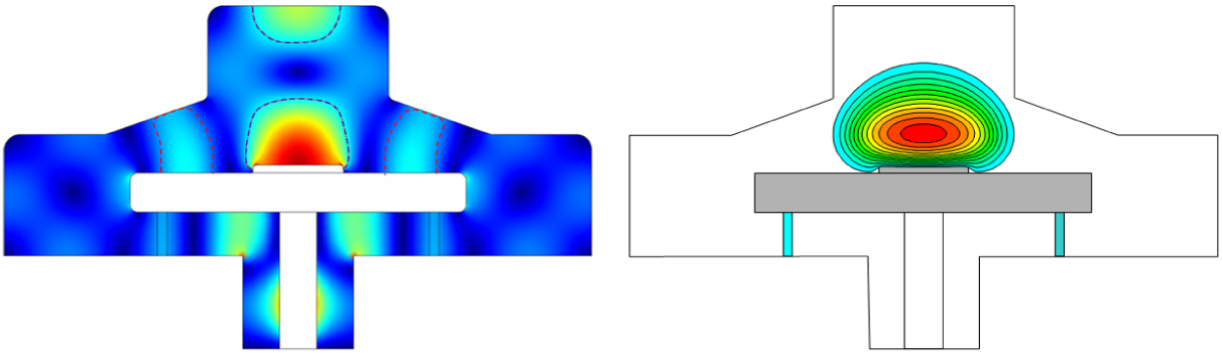

Figure 12. Illustration of the design for the second-generation ASTEX reactor [14], which makes use of a non-cylindrical resonant cavity. The main cavity mode is TM_{011} (central lobes, shown by the blue dashes in the centre of the left panel), as imposed by the central cylindrical component. Note also the secondary radial field maxima (side lobes, indicated by red dashes), typical of a TM_{021} mode (cf figure 6). In the right panel, we show modelling of a 200 mbar H_2 plasma.

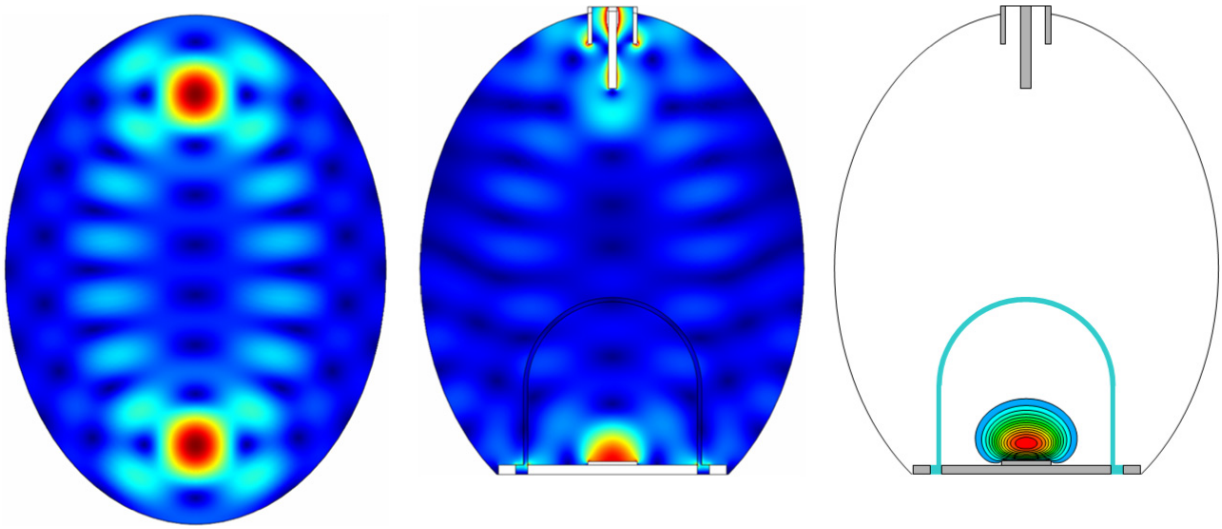

Figure 13. Illustration of the AIXTRON reactor design exploiting an ellipsoidal resonant cavity [24, 25]. The electric field structure in this cavity shows two very pronounced maxima at the two ellipsoid's foci, corresponding to the power coupling and plasma ignition locations, respectively. In the rightmost panel, we show modelling of a 200 mbar H_2 plasma.

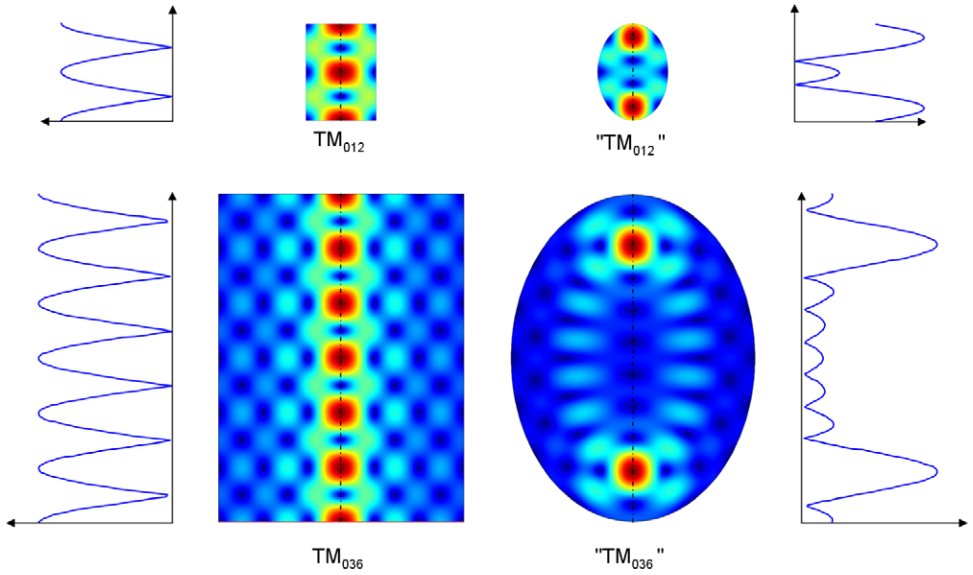

Figure 14. Evolution of the electric field structure for modes TM_{012} and TM_{036} from cylindrical (left) to ellipsoidal (right) cavities. The side graphs indicate the axial profiles of electric field strength.

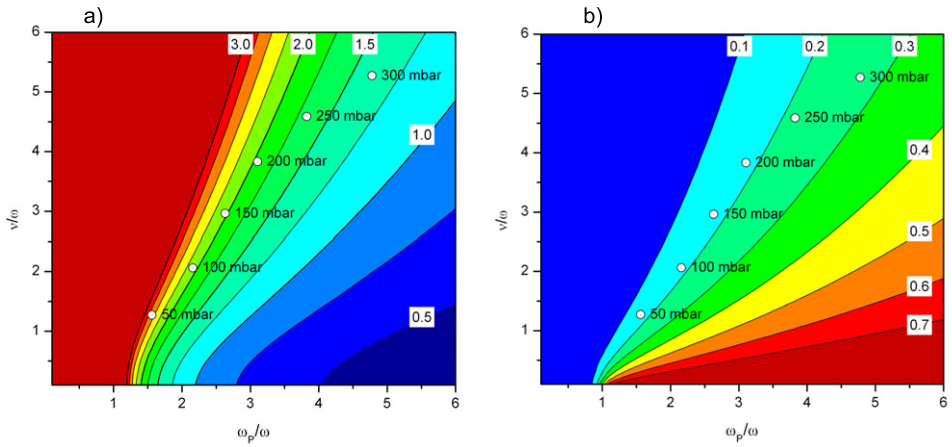

Figure 15. Evolution of the MW skin depth (in cm) at 2.45 GHz in a plasma (left) and of the power reflection coefficient (right) as a function of the (ω_P/ω) and (ν_H/ω) ratios (following [10]). The location of the operating point of the LIMHP reactor (cf figure 19), as a function of pressure, computed from the modelling results shown in figure 1, is also featured in the graphs. These values were calculated considering a point near the centre of the plasma discharge, along the cavity axis and 20 mm above the substrate surface. (a) Skin depth (cm) at 2.45 GHz and (b) power reflection coefficient.

equivalently if $\mathrm{Re}(k) \gg \mathrm{Im}(k)$. In the case where $n_e > n_c$ (one then speaks of an over-dense plasma and $\mathrm{Re}(k) \ll \mathrm{Im}(k)$), the wave amplitude is damped as $\exp[\mathrm{Im}(k)z]$. The skin depth of the wave in the plasma (δ) is then defined as [10]

$$\delta = -1/\mathrm{Im}(k) \tag{8}$$

which is determined only by the ratios ω_P/ω and ν/ω. For the MW plasmas of interest here, these parameters range typically from 1 to 5. Figure 15(a) shows the evolution of the MW skin depth at 2.45 GHz (or a wavelength of 12.2 cm) as a function of these ratios, as computed from equations (6) and (8). We note that typical skin depths are of the order of a few centimetres, which is consistent with the order of magnitude of the obtained plasma sizes. Indeed, a much smaller skin depth would prevent the penetration of the wave inside the plasma, while a larger skin depth would mean that the MW would cross the plasma without depositing any power within it.

Simulation results obtained from our self-consistent model and yielding the (ω_P, ν_H, N) quantities allow us to compute the plasma dielectric properties $(\delta, \varepsilon', \varepsilon'')$, which are reported in figure 16, for plasmas of 50 and 200 mbar pressure, respectively. We notice that the total particle density N is much smaller at the plasma centre, as a direct consequence of the discharge temperature distribution (cf figure 1). This also explains the much smaller collision frequency in the discharge core. The plasma frequency distribution is, however, directly linked to the electron density distribution (cf figure 1 and equation (2)). The ratios ω_P/ω and ν/ω provide us with the MW skin depth inside the plasma, as the pressure varies from 50 to 300 mbar (we have considered here a location

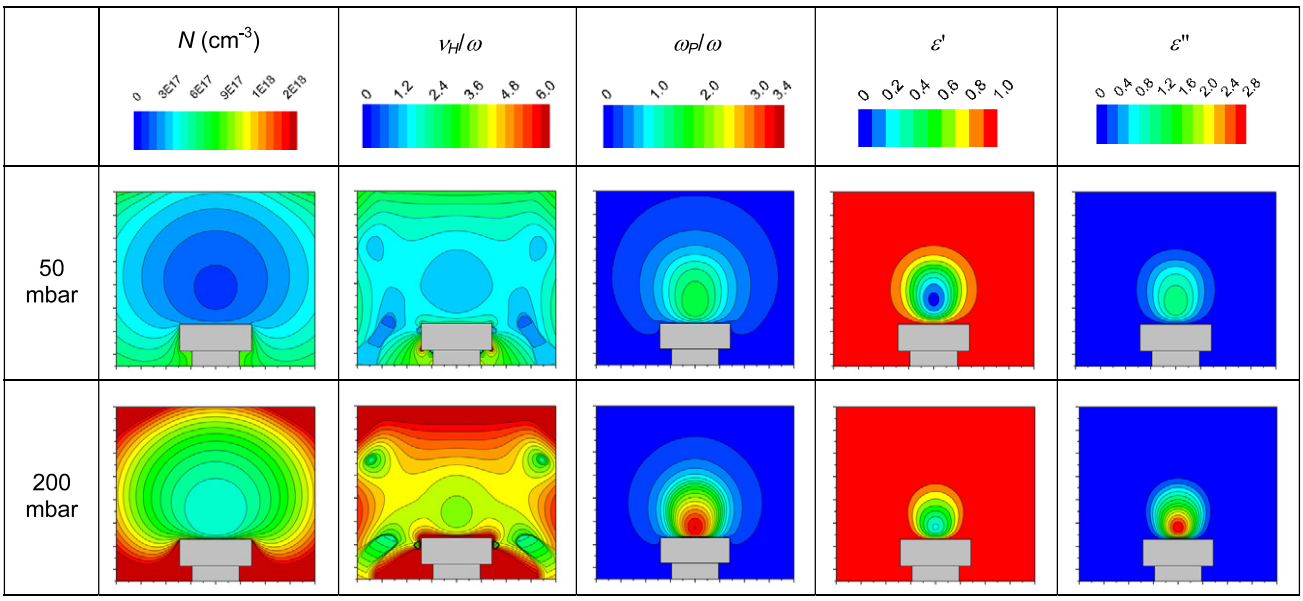

Figure 16. From left to right, spatial distribution of total particle density (N), (ν_H/ω) and (ω_P/ω) ratios, and of the normalized real (ε') and imaginary (ε'') parts of the plasma dielectric constant, in the LIMHP reactor (cf figure 19), at 50 (top row) and 200 mbar (bottom row), as determined from the plasma model (cf figure 1).

at the centre of the plasma along the reactor axis, 20 mm above the substrate surface). We see (cf figure 15) that the skin depth varies from 26 to 14 mm as the pressure is raised. The modelling results also allow us to compute the real and imaginary parts of the plasma dielectric constant ε_P, which are shown in figure 16 (at 50 and 200 mbar). The imaginary part of ε_P, responsible for the MW absorption by the plasma, varies from 1.2 at 50 mbar to nearly 2.8 at 200 mbar pressure.

The plasma can also reflect part of the incident MW power. The reflection coefficient R, defined as the ratio of the reflected power to the incident power, can be written as a function of the wavenumber k [10]:

$$R = \frac{P_R}{P_I} = \left|\frac{k_0 - k}{k_0 + k}\right|^2. \tag{9}$$

With the help of equations (6) and (7), it is possible to determine the variations of R as a function of the (ω_P/ω) and (ν/ω) ratios as shown in figure 15(b). Plasma modelling results give us the evolution of the reflection coefficient as pressure is increased from 50 to 300 mbar (at the centre of the plasma discharge, 20 mm above the substrate surface).

We find that the reflection coefficient remains small (below 20%) for pressures less than 200 mbar and increases considerably at higher pressures to reach 27% at 300 mbar. One must, however, emphasize that the relationship for R as given in equation (9) assumes an abrupt transition from 'vacuum' to the full plasma density while a more realistic ramp-up of the electron density strongly reduces the reflected power, as suggested by experimental results (where we see almost no reflected power even at high MWPD).

The plasma presence also modifies the cavity resonant frequency [27]. This mismatch becomes more and more pronounced as the power density is raised, i.e. when the electron density is increased.

In order to illustrate this effect, let us examine the case of the LIMHP first-generation reactor, designed in 1990. It is also a bell jar type reactor with a TM_{023} cavity mode as shown in figure 17. The choice of this resonance mode allows for the use of a relatively wide cavity (here 250 mm diameter), which is very useful for the implementation of spectroscopic plasma diagnostics that require, in some cases, several large access windows (four for CARS spectroscopy [21] or two for absorption spectroscopy [28]). At that time, we did not yet have the numerical tools described in this paper. This reactor was therefore tuned semi-empirically, through a relatively long and cumbersome trial-and-error process. We nevertheless observe a relatively good correlation between the electric field structure in the empty cavity and the plasma shape obtained at low pressure (25 mbar), when the plasma load does not represent a strong perturbation to the cavity behaviour. However, when we increase the microwave power density, the cavity tuning becomes more and more difficult to achieve and the reflected power, partially compensated through an impedance matching system, causes more and more pronounced heating of all the metallic walls, as shown by the thermal imaging presented in figure 18. This heating, which becomes detrimental for pressures above 150 mbar, is mainly linked to the cavity detuning due to the plasma load which had not been anticipated during the reactor design.

It is to circumvent these heat load problems that we designed a new reactor, dedicated to higher power density operations in 1994. The quartz bell jar of the first version reactor, difficult to cool, was replaced with a window located at the top of a TM_{022} cavity, which allowed us to keep the plasma diagnostic capabilities of the reactor. The MW coupling to the cavity is achieved via a circular waveguide segment at the top of which the MW is injected by an antenna (cf figure 19). The lower part of the cavity is made of a movable metallic plate

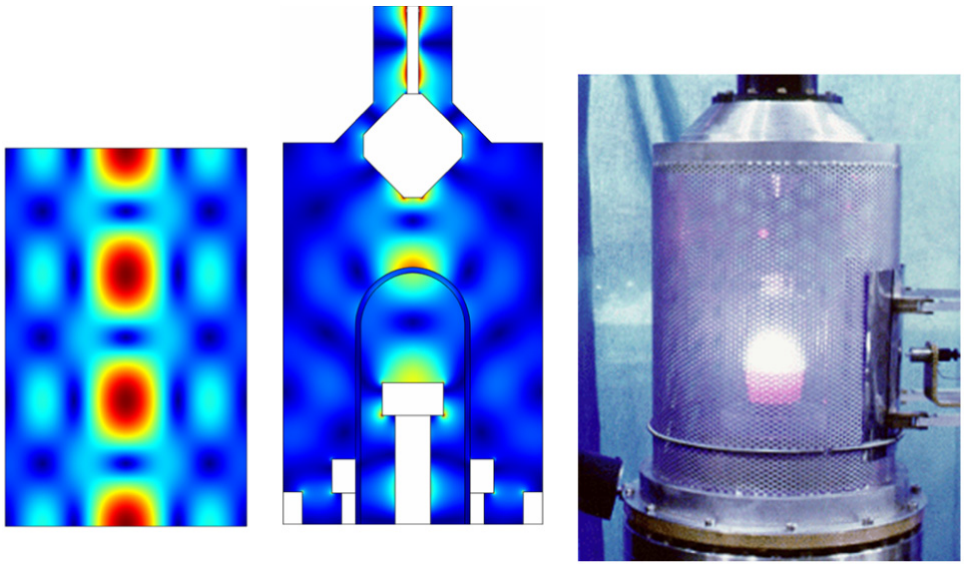

Figure 17. LIMHP bell jar reactor designed in 1990: (left) TM_{023} cavity mode; (centre) electric field distribution inside the coupled cavity with its substrate holder and quartz bell jar; (right) photograph of an H_2 plasma at 25 mbar and 600 W power.

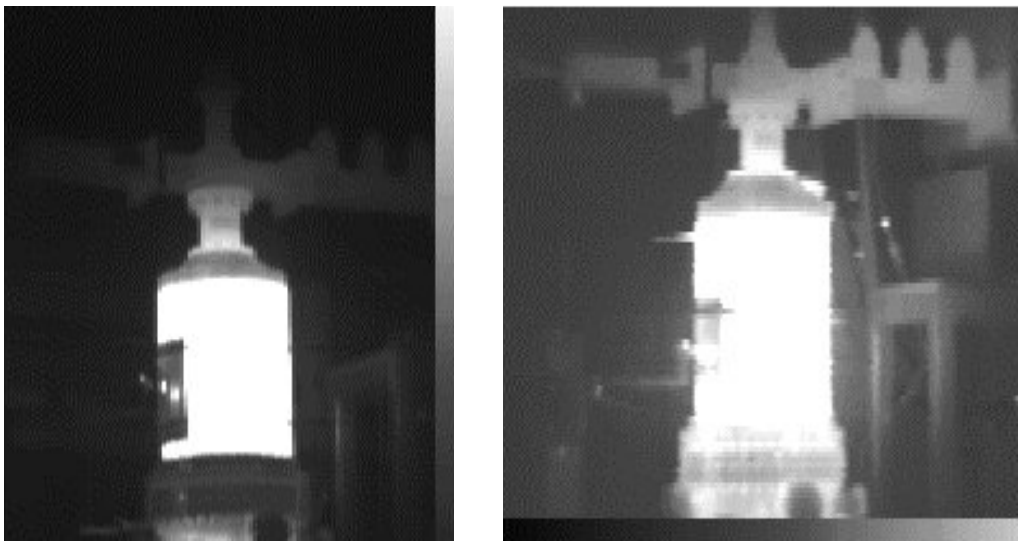

Figure 18. Thermal imaging of the bell jar reactor from figure 17, working respectively at 50 mbar (left) and 200 mbar (right) pressures. The highest temperature recorded at 200 mbar lies above 60 °C.

(in good electric contact with the vertical wall of the cavity), which enables modifying the geometrical size of the cavity and its matching. The substrate holder can be moved vertically, independently of the plate position. In order to improve the reactor heat load management, the cavity and the coupling system are entirely water-cooled through a double wall. Lastly, particular attention was paid to the quality of the vacuum in this device in order to improve the quality of the diamond films deposited.

This reactor can deliver high power density plasmas (cf figure 1), with an efficient thermal management which limits the overheating of the reactor wall. It is particularly well suited to the deposition of high purity monocrystalline diamond films [3], since in addition to the care taken about the vacuum quality inside the vessel, the plasma is relatively far from the reactor walls and the quartz window, thereby limiting potential contamination of the films. This reactor, however, still suffers from two main limitations. The first comes from the relatively small dimensions of the plasma which does not allow for deposition of diamond films homogeneously enough over surfaces larger than 40 mm in diameter. Secondly, even if the heat load problems are treated through an efficient cooling of all the walls, we still have a significant cavity mismatch at high power density. Although it is possible to modify the cavity geometry so as to considerably reduce the reflected power, the heating observed on certain parts of the waveguide and the coupling structure indicates that the MW design of the reactor

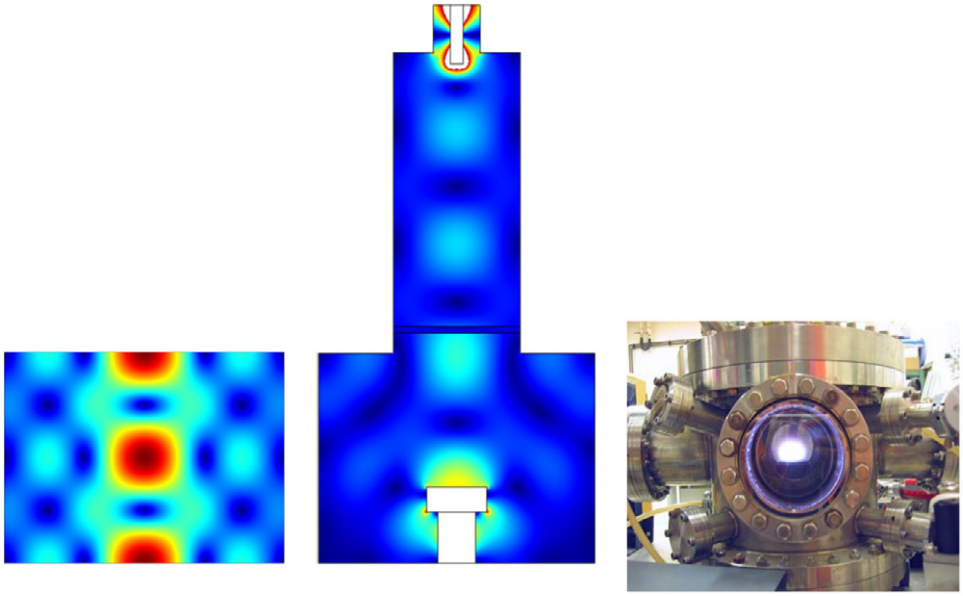

Figure 19. LIMHP stainless steel reactor designed in 1994: (left) TM_{022} cavity mode; (centre) electric field distribution inside the coupled cavity with its substrate holder and quartz window; (right) photograph of an H_2 plasma at 100 mbar.

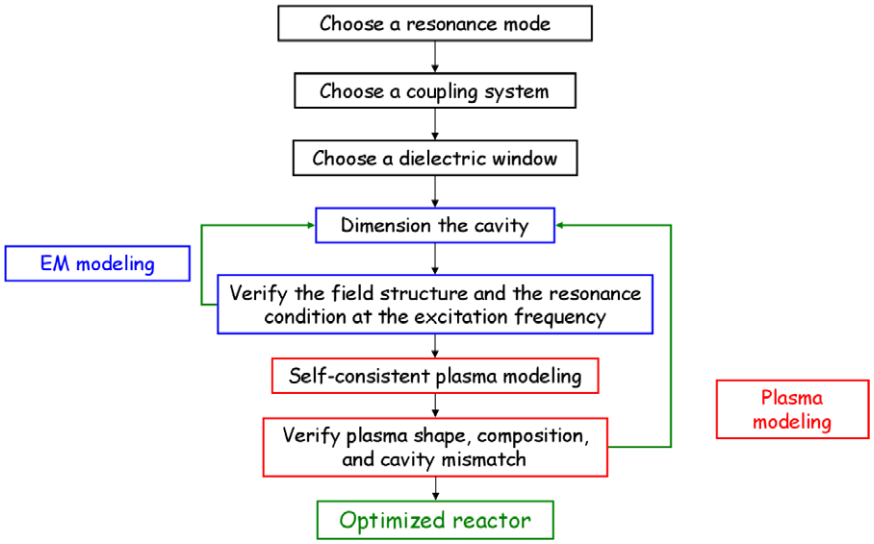

Figure 20. Design and optimization methodology for MW plasma reactors used at LIMHP, relying on electromagnetic modelling coupled to self-consistent plasma modelling.

is not optimized and that the energy efficiency of the deposition process can be still improved.

In conclusion, the strong coupling between the MW electric field distribution and the plasma requires a self-consistent treatment in order to optimize the reactor design and to obtain large size plasmas operating steadily at high MWPD.

3.5. MW plasma reactor design methodology

We have developed a methodology aiming at improving the microwave design of plasma reactors in order to facilitate stable operation for long deposition times at high power density. This method is detailed in figure 20. After having chosen the resonance mode, the coupling structure and the dielectric window (geometry and location), one proceeds with the cavity dimensioning with the help of an electromagnetic solver in order to get a cavity resonance at 2.45 GHz, while ensuring a large electric field zone in front of the substrate holder. One then solves for the plasma inside this cavity, with the help of our self-consistent model, yielding the shape and composition of the plasma, as well as the cavity detuning. If the results are not satisfactory, the cavity dimensions are modified and the process is iterated. This optimization is made under high MWPD (i.e. high pressure) discharge conditions, since correcting for detuning at low power density is usually not a problem.

We have recently undertaken such an optimization procedure on our first-generation LIMHP bell jar reactor in order to be able to use the reactor at higher power density. This study was motivated by the fact that reactors of the

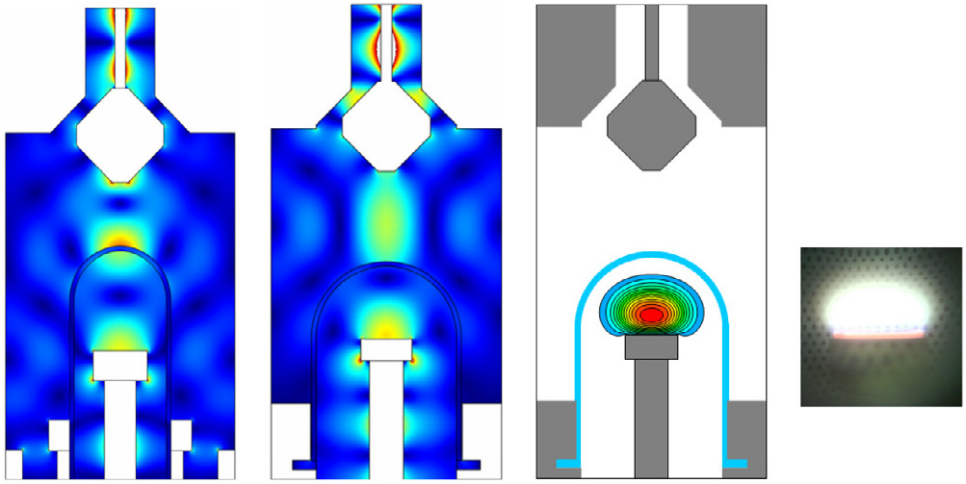

Figure 21. Optimization of the first-generation LIMHP bell jar reactor, following figure 20 (three left panels). The plasma shape coming from the self-consistent model is in perfect agreement with the experimental results (rightmost panel; pressure: 200 mbar).

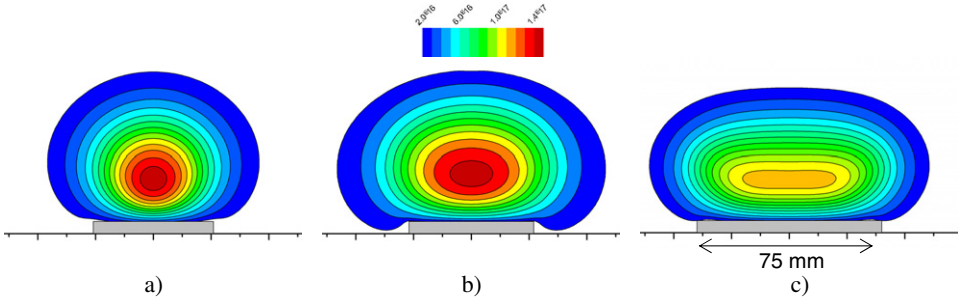

Figure 22. Evolution of the plasma shape and homogeneity (modelling of the atomic hydrogen distribution at 200 mbar) for the different generations of LIMHP reactors: (left) stainless steel reactor (1994), (centre) second-generation bell jar reactor (2007) [29], (right) third-generation reactor (2008).

bell jar type have a major advantage when one wishes to use doping impurities (such as boron or phosphorus) during growth in order to provide the deposited diamond material with semiconductor properties. Indeed, the use of boron contaminates irreversibly the reactor walls and it is then almost impossible to deposit new intrinsic diamond films even after a single exposure of the reactor to this sort of contamination. Moreover, ideally, one reactor per doping level is required if one wishes to obtain reproducible diamond films with controlled properties. In the case of bell jar type reactors, it is, however, possible to considerably reduce these memory effects by simply changing the quartz bell.

To achieve higher power operation, we have increased the diameter of the quartz bell jar to move the quartz walls away from the plasma. We also modified the cavity geometry to obtain higher power density plasma with a better radial homogeneity. The results shown in figure 21 confirm that the homogeneous plasma shape obtained experimentally is in perfect agreement with our self-consistent model predictions. This new bell jar reactor, which demonstrated excellent performance for working pressures as high as 200 mbar and good handling of heat fluxes to the walls, is now commercially available through the PLASSYS Company [29].

We have since developed a new generation of reactor at LIMHP yielding large area plasmas, working stably at very high MWPD. In addition to the attention devoted to the MW and plasma reactor design (cavity and MW coupling system optimization), we also paid particular attention to the handling of heat loads in the reactor (optimization of the cooling of the reactor's sensitive components) and to the shape and location of the quartz window. We show in figure 22 modelling results exhibiting the significant improvements obtained, both with respect to the shape and homogeneity of the plasma. The first tests performed on our prototype, at 300 mbar pressure over long deposition times (several days), have confirmed the homogeneity of the deposited films over a 3 inch diameter surface and exhibited excellent thermal load handling.

In order to increase plasma dimensions beyond 3 inches, it is necessary to lower the excitation frequency. Indeed, the size of plasma ignited in a resonant cavity is about half the MW wavelength, i.e. about 6 cm at 2.45 GHz. This dimension increases to 16 cm when the frequency is lowered to 915 MHz. Scaling up the reactors at low frequency therefore allows one to develop devices able in theory to deposit diamond on surfaces up to 6 inches in diameter.

Plasma modelling results for this 'scaled-up' prototype working at 915 MHz are reported in figure 23. They show the

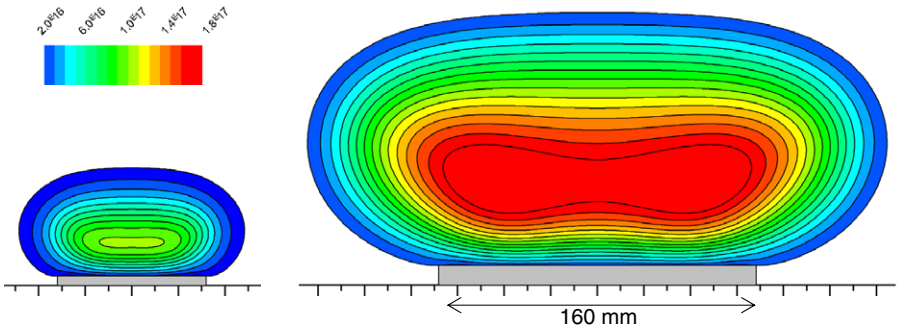

Figure 23. Evolution of the plasma shape (modelling of the atomic hydrogen distribution at 200 mbar) for the third-generation LIMHP reactor (cf figure 22) scaled up to 915 MHz (right). The figure is to scale.

distribution of atomic hydrogen that can be obtained in such a device. This reactor, which is currently being built in our laboratory, should allow us to grow diamond films on surface areas up to 160 mm in diameter.

We see in this figure that, at a pressure of 200 mbar and for optimal and stable working conditions, the atomic hydrogen density obtained at 915 MHz is almost two times higher than that obtained at 2.45 GHz. However, the MW power density in the low frequency plasma case is significantly much reduced. Indeed, the plasma volume ratio between 915 MHz and 2.45 GHz is of the order of $(160/75)^3$, i.e. about a factor of 10, if we assume a hemispherical plasma. The ratio of injected powers being 4.3, we get a power density approximately two times smaller at low frequency. Details about this surprising result (doubling of the atomic hydrogen density while halving the MWPD) will be given in a forthcoming paper.

The ratio of plasma diameters obtained at 915 MHz and 2.45 GHz is not exactly proportional to the ratio of excitation wavelengths (2.13 instead of 2.68). It is rather a function of the skin depths that characterizes the plasma obtained at the two frequencies (3.5 cm at 2.45 GHz versus 8.5 cm at 915 MHz).

To conclude, plasma excited at 915 MHz can deposit diamond on a surface area up to 4.5 times larger than plasma excited at 2.45 GHz, in conditions favourable to faster growth and better film quality. Low frequency plasma processes are therefore, from a purely economic and industrial point of view, much more interesting.

4. Conclusion

In this work, we have shown the importance of working at high pressure in order to obtain simultaneously high growth rates and high film quality.

We have also proposed a work methodology, based on careful electromagnetic and plasma modelling, that yields high density, large area plasmas. However, important heat fluxes to the walls linked to the use of high power density plasma require efficient cooling of sensitive reactor components and optimization of the microwave coupling structure as well as the shape and location of the dielectric window inside the cavity. The substrate holder must also be carefully designed to provide precise control of the surface temperature, which becomes particularly challenging at high pressure.

This methodology was successfully used in our laboratory. It allowed us to obtain reactors that work stably, at high pressure (300 mbar), and that can deposit homogeneous films over up to 75 mm diameter surfaces, at 2.45 GHz. The first tests undertaken on a prototype fully validated the predictions made by our plasma model. Scaling up to 915 MHz has revealed the potentialities of low frequency reactors for industrial uses. Such a new device is currently being built in-house and experimental tests of the modelling need to be performed in order to definitely state the advantages of low frequency operation.

Acknowledgment

The Délégation Générale pour l'Armement (DGA) is thanked for financial support, through contract no. 02 34 070.

References

[1] Isberg J, Hammersberg J, Johansson E, Wikstrom T, Twitchen D J, Whitehead A J, Coe S E and Scarsbrook G A 2002 *Science* **297** 1670
[2] Kasu M and Kobayashi N 2003 *Diamond Relat. Mater.* **12** 413
[3] Achard J, Silva F, Tallaire A, Bonnin X, Lombardi G, Hassouni K and Gicquel A 2007 *J. Phys. D: Appl. Phys.* **40** 6175
[4] Gaukroger M P, Martineau P M, Crowder M J, Friel I, Williams S D and Twitchen D J 2008 *Diamond Relat. Mater.* **17** 262
[5] Silva F, Achard J, Bonnin X, Brinza O, Michau A, Secroun A, De Corte K, Felton S, Newton M and Gicquel A 2008 *Diamond Relat. Mater.* **17** 1067
[6] Harris S J 1990 *Appl. Phys. Lett.* **56** 2298
[7] Harris S J and Goodwin D G 1993 *J. Phys. Chem.* **97** 23
[8] Goodwin D G 1993 *J. Appl. Phys.* **74** 6888
[9] Hassouni K, Grotjohn T A and Gicquel A 1999 *J. Appl. Phys.* **86** 134
[10] Hagelaar G J M, Hassouni K and Gicquel A 2004 *J. Appl. Phys.* **96** 1819
[11] Hassouni K, Silva F and Gicquel A 2009 *J. Phys. D: Appl. Phys.* submitted
[12] Lombardi G, Hassouni K, Stancu G D, Mechold L, Röpcke J and Gicquel A 2005 *J. Appl. Phys.* **98** 053303
[13] Silva F, Achard J, Brinza O, Bonnin X, Hassouni K, Anthonis A, De Corte K and Barjon J 2009 *Diamond Relat. Mater.* **18** 683–97
[14] Besen M M, Sevillano E and Smith D K 1996 *Patent Specification* 5,501,740

[15] Asmussen J and Zhang J 1994 *Patent Specification* 5,311,103
[16] Tan W and Grotjohn T A 1994 *J. Vac. Sci. Technol.* A **12** 1216
[17] Gaudreau M P J 1989 *Patent Specification* 4,866,346
[18] Darras D, Rius J. M, Chollet P, Boutroy N, Beldi N and Oge F 2004 *Patent Specification* 6800346
[19] Silva F, Michau A, Bonnin X, Gicquel A, Boutroy N, Chomel N and Desoutter L 2007 *Diamond Relat. Mater.* **16** 1278
[20] Tallaire A, Achard J, Silva F and Gicquel A 2005 *Phys. Status Solidi* a **202** 2059
[21] Gicquel A, Hassouni K, Farhat S, Breton Y, Scott C D and Lefebre M 1994 *Diamond Relat. Mater.* **3** 581
[22] Pleuler E, Wild C, Funer M and Koidl P 2002 *Diamond Relat. Mater.* **11** 467
[23] Spitzl R 2001 *Patent Specification* 6.198.224
[24] Wild C, Funer M and Koidl P 1999 *Patent Specification* 5,954,882
[25] Funer M, Wild C and Koidl P 1999 *Surf. Coat. Technol.* **116–119** 853
[26] Lieberman M A and Lichtenberg A J 1994 *Principles of Plasma Discharges and Material Processing* (New York: Wiley)
[27] Stoffels E, Stoffels W W, Vender D, Kando M, Kroesen G M W and de Hoog F J 1995 *Phys. Rev.* E **51** 2425
[28] Lombardi G, Hassouni K, Stancu G. D, Mechold L, Röpcke J and Gicquel A 2005 *Plasma Sources Sci. Technol.* **14** 440
[29] Plassys http://www.plassys.com/